Supporting Information

Cobalt oxide/cerium oxide heterogeneous interfaces as advanced durable and bifunctional electrocatalyst for robust industrial relevant overall water splitting

Akbar I. Inamdar*[a], Amol S. Salunke[a], Jun Ho Seok[b], Harish S. Chavan[a], Nabeen K. Shrestha[a], Sang Uck Lee*[b], Sangeun Cho*[a], Hyunsik Im[a]

[a]Division of System Semiconductor, College of AI Convergence, Dongguk University, Seoul, 04620, Republic of Korea.

[b] School of Chemical Engineering, Sungkyunkwan University, Suwon 16149, Republic of Korea

*Corresponding Authors

*E–mail: akbarphysics2002@gmail.com (A. I. I.), suleechem@skku.edu (S. U .L.), sangeun.c@dongguk.edu (S. C.)

Table S1. Literature survey and comparison of various electrocatalysts in terms of the OER, HER, and cell voltages required to reach a current density of 10 mAcm^{-2}.

Sr. No	Catalysts	Cell Voltage (V) @10mAcm^{-2} KOH or NaOH	η (mV) @10mAcm^{-2} In KOH or NaOH		Ref.
			OER	HER	
1.	NiFe LDH-NS@DG10 hybrid catalyst	1.5 @20mAcm^{-2} (1 M KOH)	210 @10mAcm^{-2}	115 @20mAcm^{-2}	[1]
2.	Nonprecious CuFe Composite	1.64 (1 M KOH)	218	158	[4]
3.	defect-rich ultrathin Co(OH)$_2$ (D-U-Co(OH)$_2$)	-	223	-	[8]
4.	Nanosized CoNi Hydroxide@Hydroxysulfide	-	274 (0.10 M KOH)	-	[9]
5.	Boronized NiFe	-	309 (1 M KOH)	-	[10]
6.	V-doped Ni$_3$S$_2$ nanowire	-	-	39 (1 M KOH)	[12]
7.	Ru single-atom on cobalt-iron bimetallic-alloy encapsulated by graphitic carbon (RuSACoFe$_2$/G)	1.48 (1M KOH)	180	129	[14]
8.	CoN nanowire	-	290 (1 M KOH)	-	[15]
9.	Highly densed NiS-CoS nanorod arrays	1.47 (1 M KOH)	F170	102	[16]
10.	nickel iron diselenide	-	195 (1 M KOH)	-	[17]
11.	Carbon coated porous nickel phosphides nanoplates	-	300 (1 M KOH)	-	[18]
12.	Fe-doped Ni$_3$Se$_4$ ultrathin nanosheets	1.60 (1M KOH)	225	173	[19]
13	Fe-doped Co$_3$O$_4$ hierarchical NPs composed of ultrathin nanosheets	-	262	-	[21]
14.	Au-doped Co-Ni Hydroxide	1.75 (1M NaOH) 1.9 (6 M NaOH)	340	200	[25]
15.	Anion insertion enhanced NiCeO$_x$H$_y$	-	177	-	[26]
16.	Nickel-Chromium Layered Double Hydroxide (NiCr-LDH)	1.55 (1M KOH)	319 @ 100mAcm^{-2}	138 @ 100mAcm^{-2}	[27]

17	NiFe and CoFe -LDHs	-	348 (NiFe) 404 (CoFe)	-	[28]
18.	Self-supported NiMo-based nanowire arrays	1.507 (1M KOH)	230	22	[29]
19.	N-doped graphene layer coated Fe-Ni alloy nanoparticles encapsulated within an N-doped carbon hollow nanobox	1.701 (1M KOH)	270	201	[30]
20.	Phase-pure pentlandite $Ni_{4.3}Co_{4.7}S_8$ binary sulfide	1.67 (1M KOH)	133.8 @20mAcm^{-2}	148 @10mAcm^{-2}	[31]
21.	Nickel−Iron/Nanocarbon Hybrids	1.58 (1M KOH)	330	219	[32]
22.	$Ni(OH)_2/Ni_3S_2$ hybrid nanosheet arrays	1.57 (1M KOH)	270 @20mAcm^{-2}	200	[33]
23.	NiCo-LDH	-	293 (0.1M KOH)	-	[34]
24.	Enabling and Inducing Oxygen Vacancies in Se@CoFe-LDH	-	251 1M KOH @ 50mAcm^{-2}	222 0.5M H_2SO_4 50mAcm^{-2}	[35]
25.	Ce-Doped NiFe -LDH	-	227	-	[36]
26.	Bimetallic iron-iridium alloy nanoparticles/NF (FeIr/NF)	1.48 (1M KOH)	200 @ 20mAcm^{-2}	16.6 @ 20mAcm^{-2}	[37]
27.	FeNiSSe nanotube	1.56 (1M KOH)	213	91.2	[38]
28.	CoNiP-CoNi alloy	1.76 (1M KOH)	300	150	[39]
29.	Ni-Co-Fe mixed sulfide ultrathin nanosheets on Ni nanocones	1.54 (1M KOH)	207	106	[40]
30.	porous $Co_{0.75}Ni_{0.25}(OH)_2$ nanosheets	1.56 (1M KOH)	235	94	[41]
31.	Co–Ni–B	1.72 (1M KOH)	313	205	[42]
32.	NiCo-LDH	1.66 (1M KOH)	271	162	[43]
33.	p-NFNR@Ni−Co−P	1.62 (1M KOH)	272	125	[44]
34.	Ni–Co–P	1.62 (1M KOH)	270	107	[45]
35.	$Co(OH)_2$@NCNTs	1.72 (1M KOH)	270	170	[46]
36.	Mo-$NiCo_2O_4$/$Co_{5.47}$N/NF	1.56 (1M KOH)	270 @50mAcm^{-2}	170 @50mAcm^{-2}	[47]

37.	nickel–cobalt bimetal phosphide	1.59 (1M KOH)	245	129	[48]
38.	NiV LDH	-	200	-	[79]
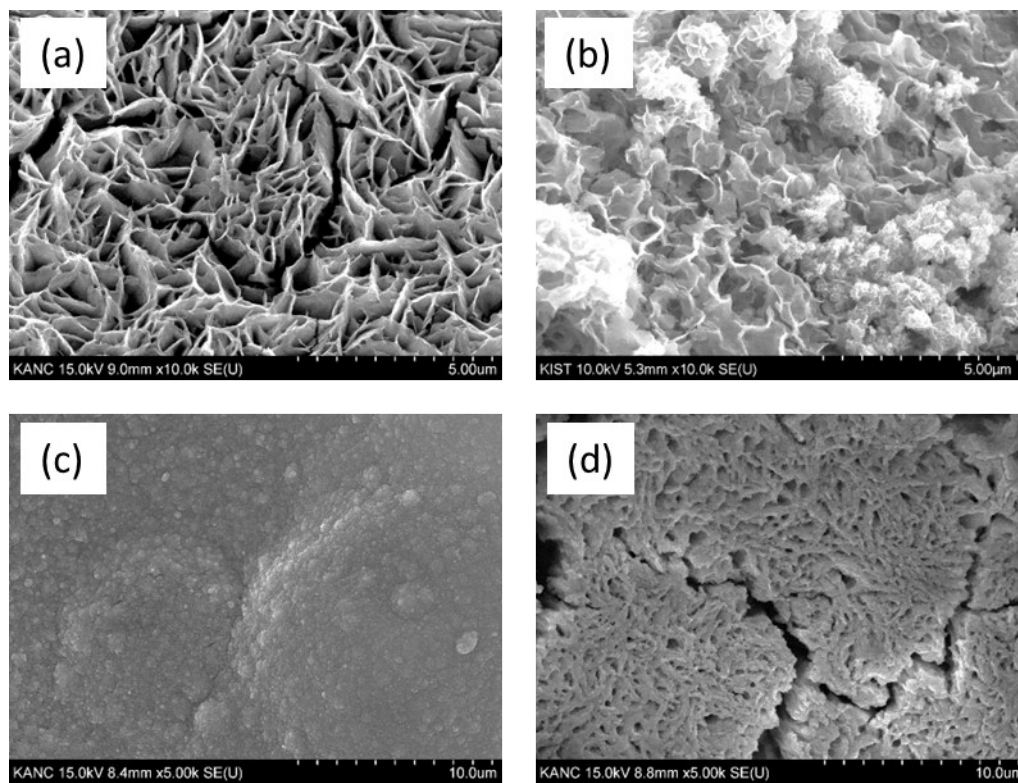
Fig. S1. Low-magnification SEM images of **(a)** $Co(OH)_2$, **(b)** $Co_{0.85}Ce_{0.15}$, **(c)** $Co_{0.50}Ce_{0.50}$, **(d)** CeO_2.
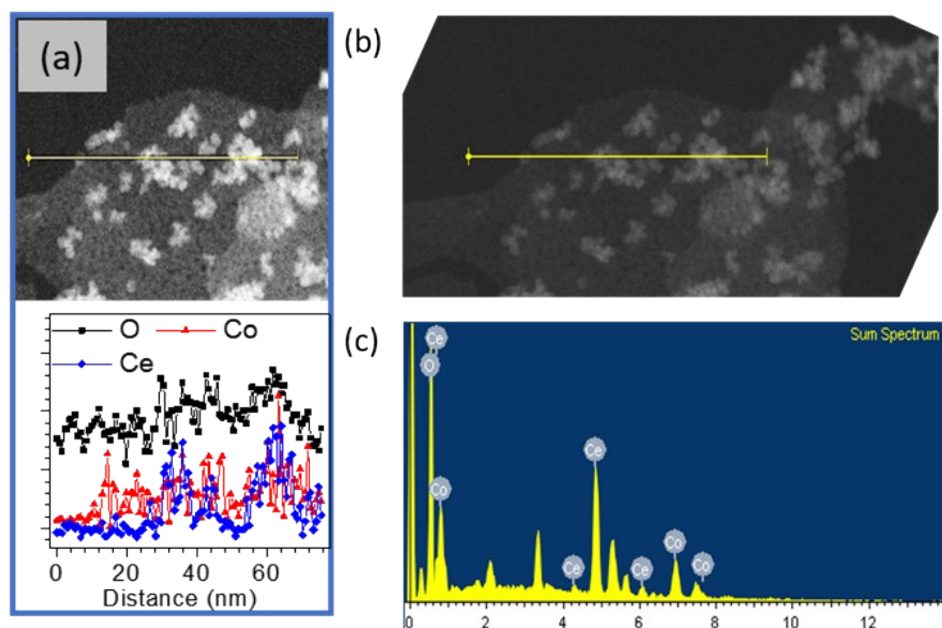
Fig. S2. (**a**) Line-scanning profiles of O, Ce and Ce along the line in the STEM image (scale bar is 75nm), (**b, c**) EDX elemental analysis of the $Co_{0.85}Ce_{0.15}$ showing its chemical composition characteristics.

Table S2. Elemental analysis using EDAX for the sample $Co_{0.85}Ce_{0.15}$.

Element	Wt%	Atomic %
O	25.38	64.67
Co	33.99	23.51
Ce	40.63	11.82

Table S3 Amount of the Co and Ce in percentage determined via ICP-MS measurements

Sample Name	59 Co [He]		140 Ce [No gas]	
	Concentration *ppm(μg/g)*	RSD (%)	Concentration *ppm(μg/g)*	RSD (%)
$Co_{0.95}Ce_{0.05}$	103180.892	3.5	123897.332	0.3
$Co_{0.85}Ce_{0.15}$	27528.358	1.1	86966.297	0.1
$Co_{0.75}Ce_{0.25}$	11861.818	0.6	92447.590	1.3
$Co_{0.50}Ce_{0.50}$	95243.324	0.3	9433.036	1.0
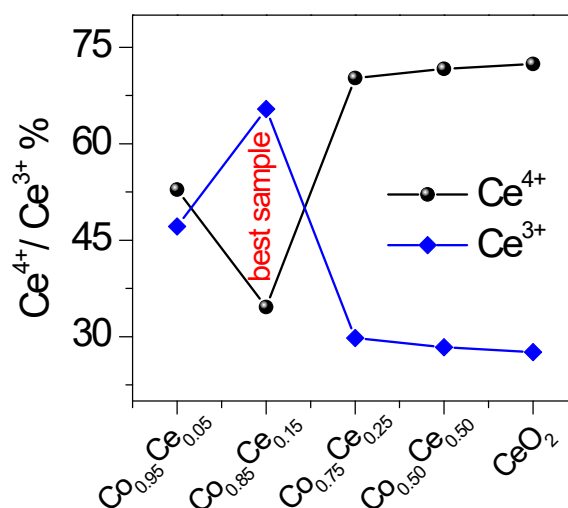
Fig. S3. Variation in the Ce oxidation state in $Co_{1-x}Ce_x$, (where x = 0.05, 0.15, 0.25, and 0.50) and CeO_2 catalysts analysed using XPS.
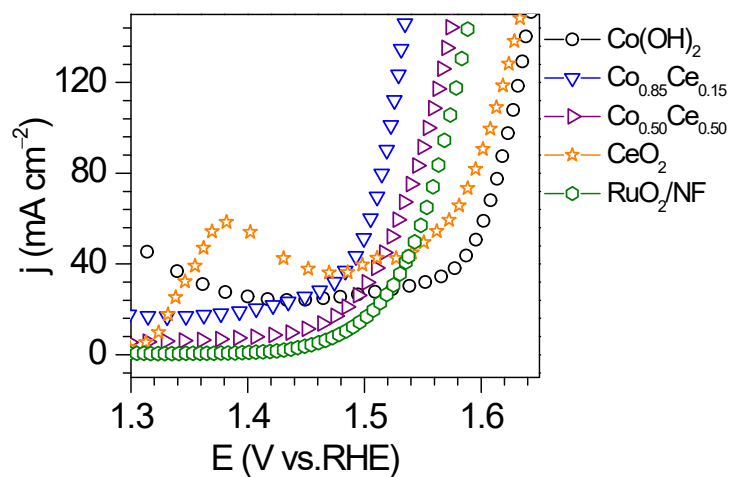
Fig. S4. Enlarged view of the *iR*-corrected LSV curves of Co(OH)$_2$, Co$_{1-x}$Ce$_x$ (where x = 0.15 and 0.50), and CeO$_2$ catalysts recorded in a 1M KOH electrolyte at a scan rate of 5 mVs^{-1} for the OER.
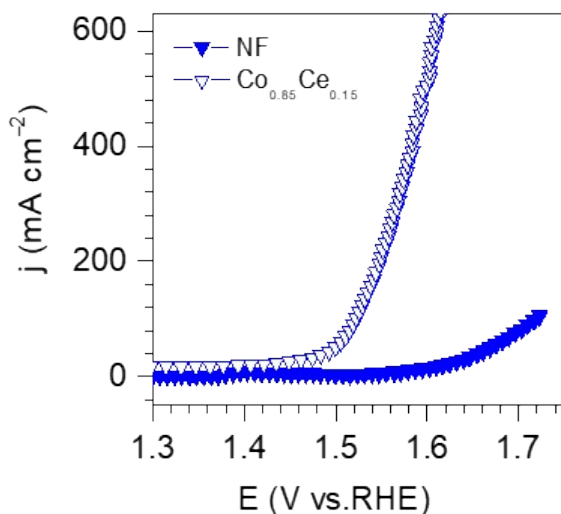
Fig. S5. *iR*-corrected LSV curves for the Ni foam in comparison with Co$_{0.85}$Ce$_{0.15}$ to determine the contribution of Ni foam to OER activity.

1.1 Conversion equations for an SCE to an RHE

$$E(RHE)=E_{1(SCE)} + E_{0(SCE)} + 0.0591pH \qquad (1)$$

where E_1 is the actual measured potential and E_0 is the standard potential for the SCE (0.241 V). The pH of the 1 M KOH electrolyte was 13.68.

$$E_{(RHE)} = E_{1(SCE)} + 0.241 + 0.0591*(13.68)$$

$$E_{(RHE)} = E_{1(SCE)} + 0.241 + 0.809$$

$$E_{(RHE)} = E_{1(SCE)} + 1.05$$

Table S4. Electrochemical parameters including the overpotential at different current densities and Tafel slopes for $Co(OH)_2$, $Co_{1-x}Ce_x$, and CeO_2 catalysts in relation to the OER.

Sample	Overpotential (mV)		Tafel slope (mV dec^{-1})	Mass activity (Ag^{-1})
	@100mAcm^{-2}	@500mAcm^{-2}		
$Co(OH)_2$	393.4	478.9	109.7	1.95
$Co_{0.85}Ce_{0.15}$	**291.6**	**368.1**	**85.02**	**11.77**
$Co_{0.50}Ce_{0.50}$	324.1	429.6	120.0	8.76
CeO_2	378.0	518.0	165.7	5.60

1.2 Electrochemical surface area analysis of the $Co_{1-x}Ce_xO$ catalysts
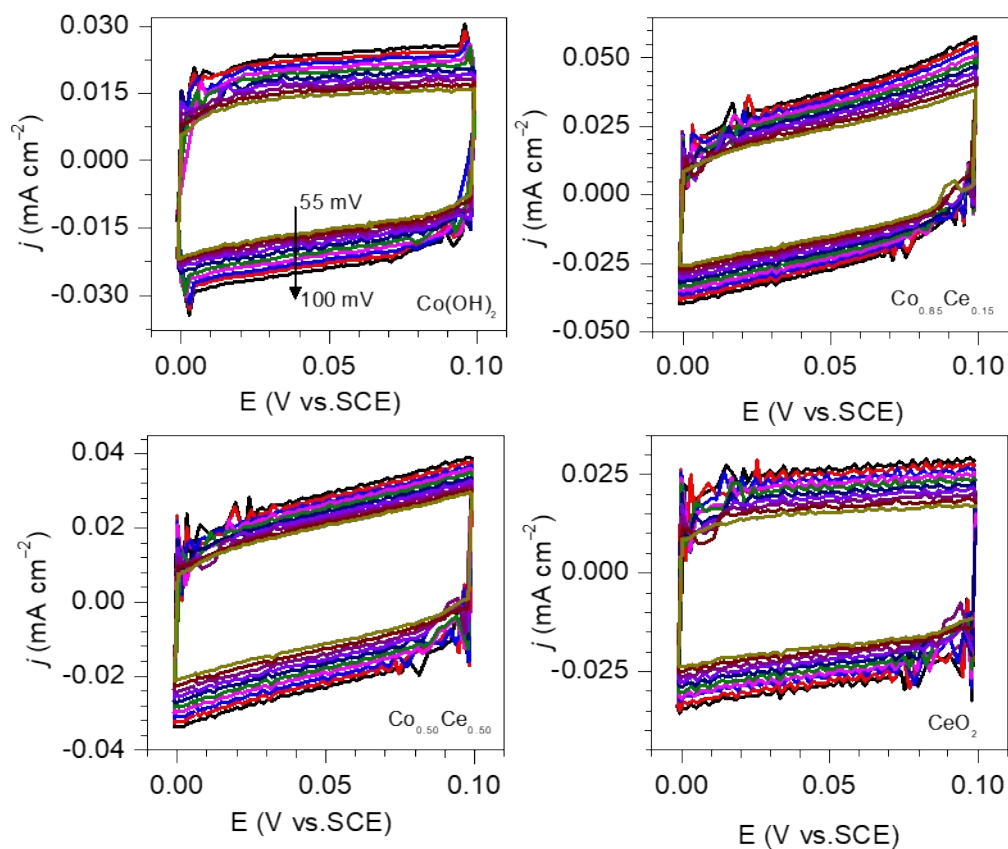
The ECSA of the $Co(OH)_2$, $Co_{1-x}Ce_x$, and CeO_2 catalysts was estimated using CV curves measured at different scan rates in the non-Faradaic voltage region. **Fig. S6(a)** presents the CV curves for catalysts recorded at a scan rate of 55, 60, 70, 75, 80, 85, 90, 95, and 100 mVs^{-1}. The ECSA of the catalyst was calculated using Eq. (2):[S1,S2]

$$ECSA = C_{dl}/ C_s \qquad (2)$$

where C_S is the specific capacitance in an alkaline medium (0.040 mF cm^{-2} for the KOH electrolyte) and C_{dl} is the specific capacitance of the double-layer region. The slope of the capacitive current (Δj), measured at a non-Faradaic voltage of 0.05 V versus the scan rate (**Fig. S6b**), was used to obtain the ECSA of the catalyst. The double-layer capacitance and ECSA of the $Co_{1-x}Ce_x$ samples are presented in **Table S5**. To accurately evaluate the intrinsic OER catalytic activity, we normalized the LSV curves for $Co(OH)_2$, $Co_{1-x}Ce_x$, and CeO_2 catalysts by the ECSA.

Table S5. Estimation of the double-layer capacitance and ECSA from the CV curves recorded at different scan rates in the non-Faradaic voltage region for mixed phase $Co(OH)_2$, $Co_{1-x}Ce_x$ oxides, and CeO_2.
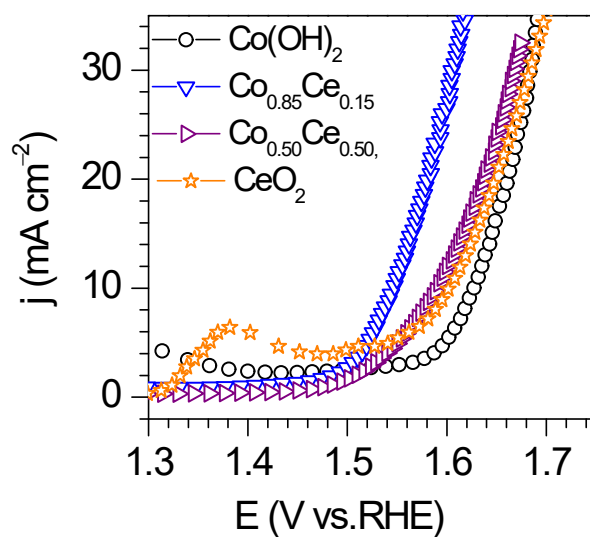
Sample	Double-layer capacitances ($\mu F\ cm^{-2}$)	ECSA (cm$^{2)}$
$Co(OH)_2$	0.208	5.2
$Co_{0.85}Ce_{0.15}$	0.300	7.5
$Co_{0.50}Ce_{0.50}$	0.192	4.8
CeO_2	0.234	5.85

Fig. S6. **(a)** CV curves for Co(OH)$_2$, Co$_{1-x}$Ce$_x$, (where x = 0.15, and 0.50) and CeO$_2$ catalysts recorded at a scan rate of 55, 60, 65, 70, 75, 80, 85, 90, 95 and 100 mVs^{-1}.
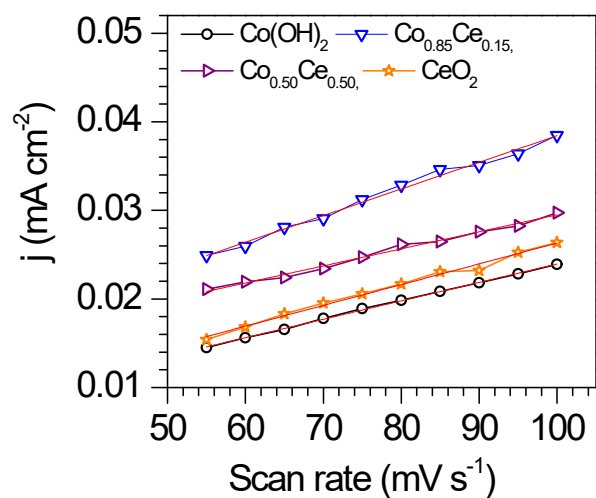
Fig. 6(b). Slope of the capacitive current (Δj) measured at a non-Faradaic voltage of 0.05 V versus the scan rate.

Fig. S7. The LSV curves of the $Co(OH)_2$, $Co_{1-x}Ce_x$, and CeO_2 catalysts in which the current density is normalized with the ECSA values.

## 1.3 Electrochemical impedance spectroscopy analysis of the $Co_{1-x}Ce_x$ catalysts

Electrochemical impedance spectroscopy (EIS) measurements were carried out to elucidate the electrocatalytic activity of the $Co(OH)_2$, $Co_{1-x}Ce_x$, and CeO_2 catalysts. **Figure S8** presents the measured Nyquist plots for the $Co_{1-x}Ce_x$, pure $Co(OH)_2$, and pure CeO_2 catalysts and the corresponding equivalent circuit diagram. The Nyquist plots exhibited a small semi-circle in the high-frequency region and a straight line in the low-frequency region, which were associated with the charge-transfer resistance (R_2) and Warburg impedance, respectively. The Nyquist curves were modelled using the equivalent circuit diagram (**Fig. S8**), in which R_1 is the solution resistance, R_2 is the charge-transfer resistance, and W_0 is the Warburg impedance. The values for R_1 and R_2 estimated from the Nyquist plots are presented in **Table S6**. It was found that $Co_{0.85}Ce_{0.15}$ had the lowest charge-transfer resistance (0.087Ω), which was much lower than that of the other catalysts. This low charge-transfer resistance and the fast kinetics of $Co_{0.85}Ce_{0.15}$ were in accordance with its superior OER activity.
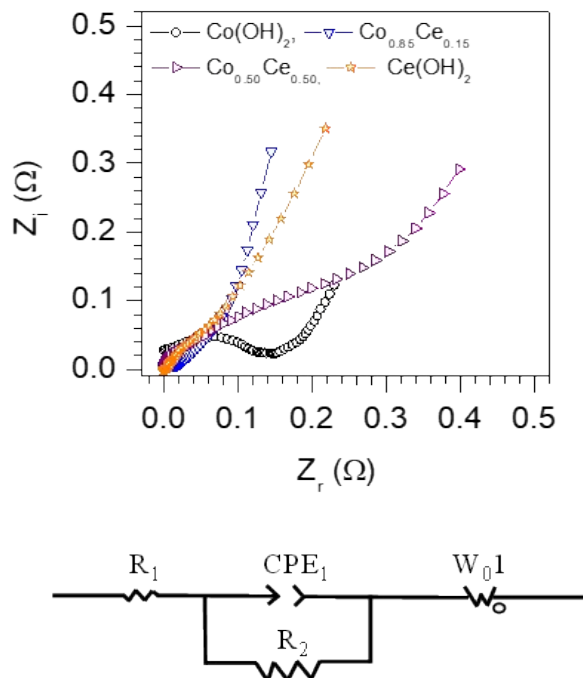
Fig. S8. Nyquist plots (normalized to zero- on the x-axis) for the $Co(OH)_2$, $Co_{1-x}Ce_x$ (where x =0.15, and 0.50), and CeO_2 catalysts recorded at a 0-bias voltage and the equivalent circuit diagram used to fit the curves.

Table S6. EIS fitting parameters for the $Co(OH)_2$, $Co_{1-x}Ce_x$ (where x = 0.15, and 0.50), and CeO_2 catalysts.

| Sample	$R1$ (Ω)	$R2$ Ω
$Co(OH)_2$	0.91	0.12
$Co_{0.85}Ce_{0.15}$	0.87	0.087
$Co_{0.50}Ce_{0.50}$	1.07	0.33
CeO_2	0.92	0.56
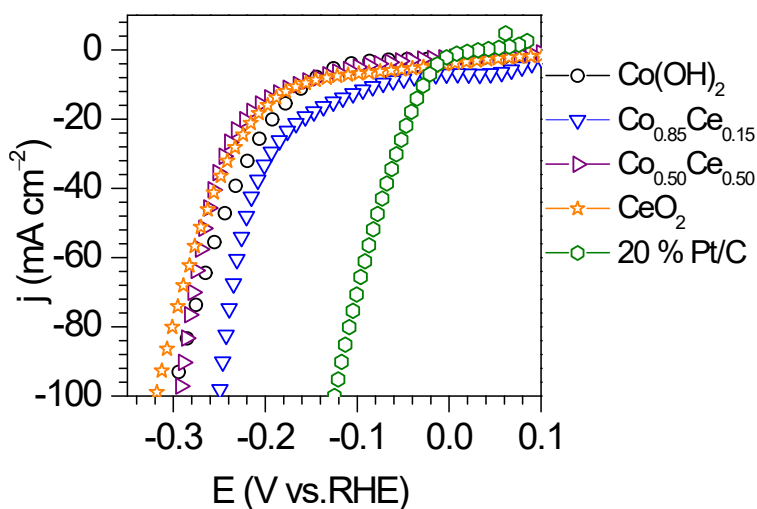
Fig. S9. Magnified view of the *iR*-corrected LSV curves recorded in a 1M KOH electrolyte at a scan rate of 5 mVs^{-1} for the HER for the $Co(OH)_2$, $Co_{1-x}Ce_x$ (where x = 0.15, and 0.50), , and CeO_2 catalysts.

Table S7. Comparison of the HER overpotential and Taffel slope of the $Co(OH)_2$, $Co_{1-x}Ce_x$ (where x = 0.15, and 0.50), and CeO_2 catalysts.

Sample	Overpotential (mV) @ 10mAcm^{-2}	Overpotential (mV) @ 400mAcm^{-2}	Tafel slope (mV dec^{-1})
$Co(OH)_2$	155.6	489.9	153.8
$Co_{0.85}Ce_{0.15}$	**76.27**	**301.1**	**92.4**
$Co_{0.50}Ce_{0.50}$	163.8	354.0	142.7
CeO_2	169.6	491.6	154.7

**Table S8**. The concentrations of the Co and Ce species detected after the stability tests via ICP-MS analysis

Electrolyte	56 Fe [H2] Concentration *ppm(µg/g)*	RSD	59 Co [He] Concentration *ppm(µg/g)*	RSD	140 Ce [No gas] Concentration *ppm(µg/g)*	RSD
Before stability KOH	0.027	5.6	0.003	7.8	ND	
After stability KOH	0.026	1.9	0.008	3.8	ND	
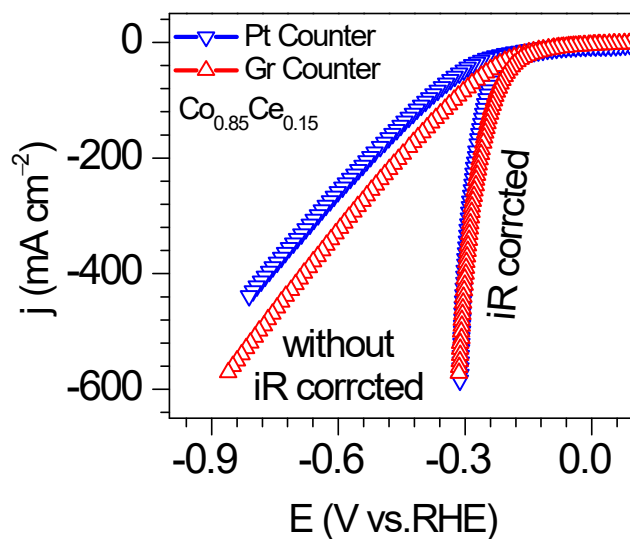
Fig. S10. HER polarization curves of the $Co_{0.85}Ce_{0.15}$ catalyst with Pt and Graphite (Gr) as a counter electrode.
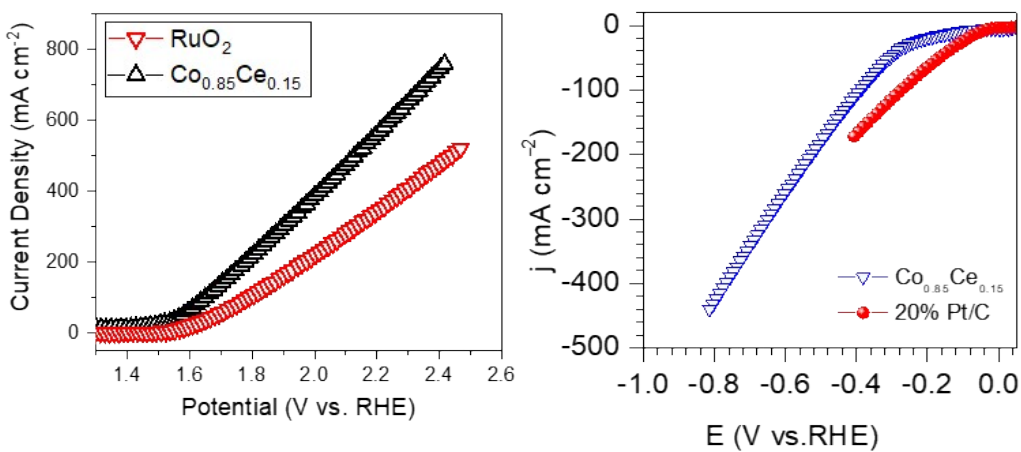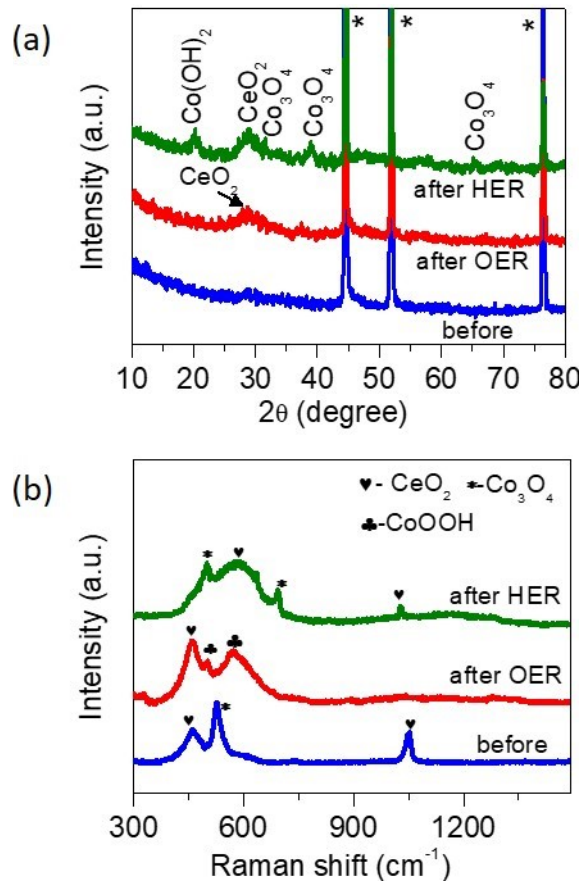

Fig. S11. Without iR-correction OER and HER polarization curves of the $Co_{0.85}Ce_{0.15}$, RuO_2/NF and 20 % Pt/C in 1M KOH electrolyte.
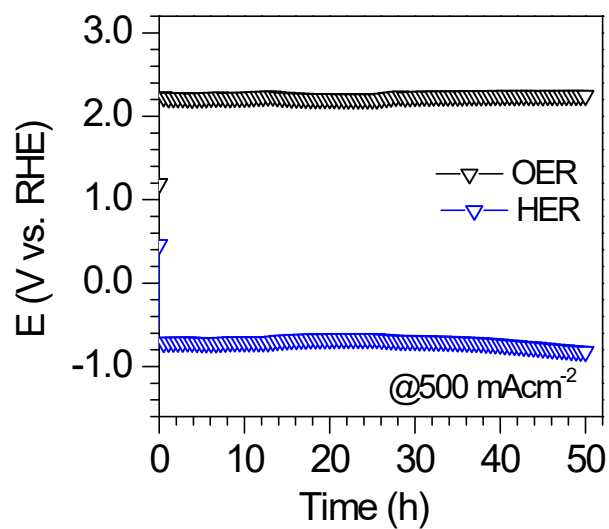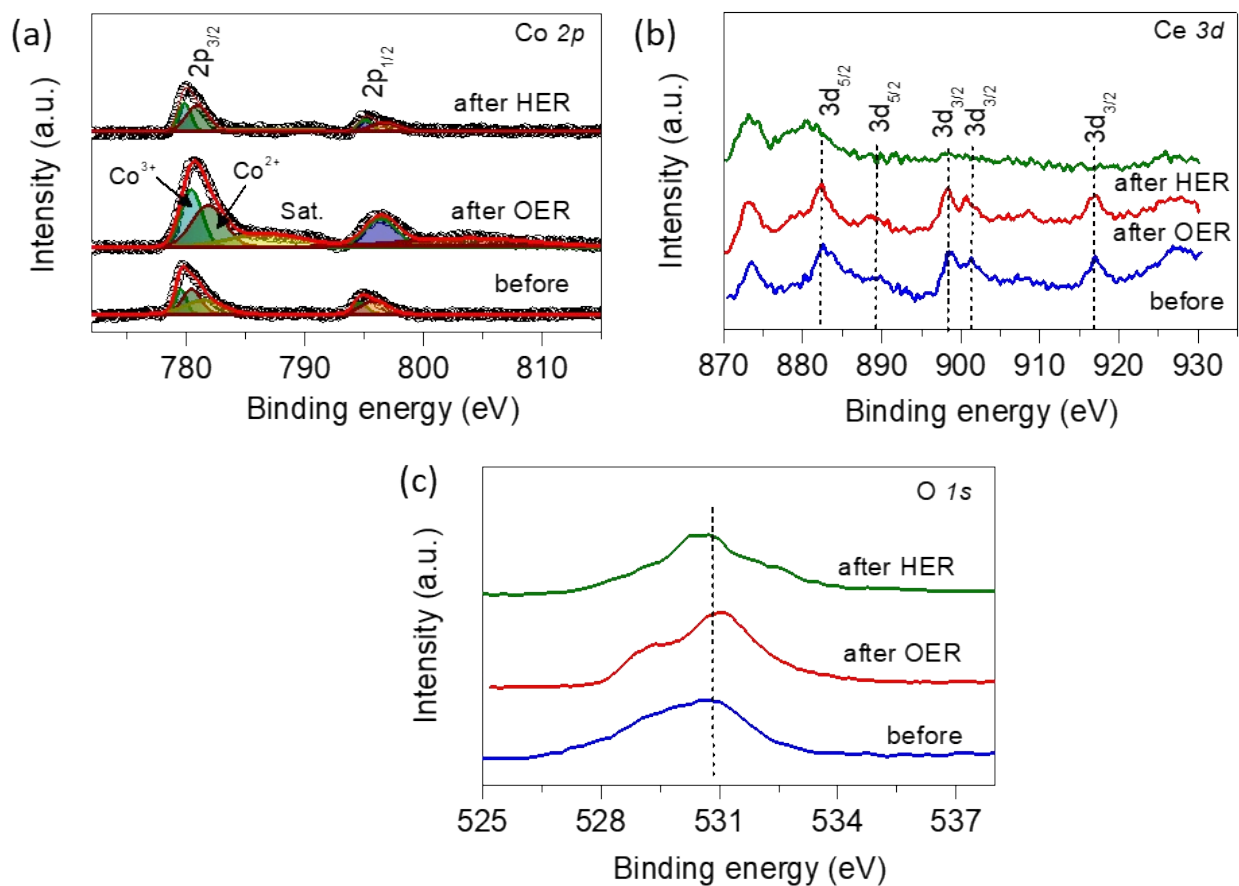
Fig. S12. Chronopotentiometry stability curve (without iR- correction) of best performing $Co_{0.85}Ce_{0.15}$ sample at current density of 500-mA cm^{-2} for 50 hours of continuous operation
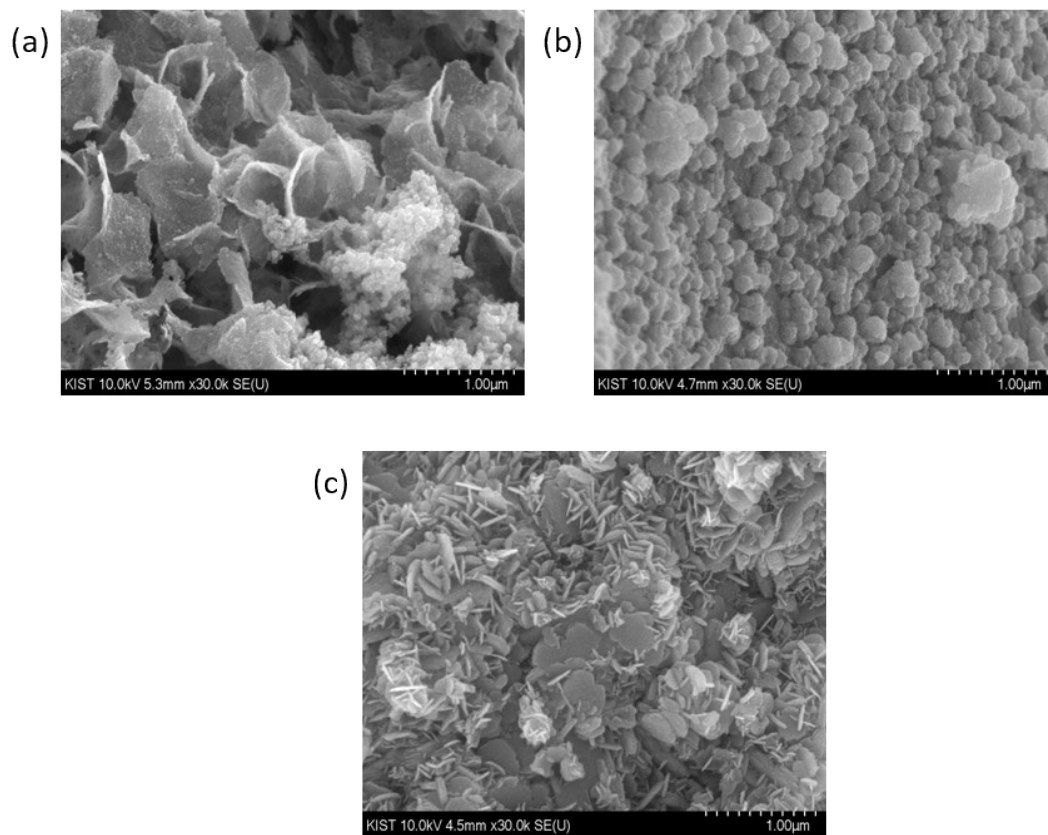
Fig. S13. Influence of long-term OER and HER measurements on the structural properties of $Co_{0.85}Ce_{0.15}$ monitored using **(a)** XRD and **(b)** Raman analysis before and after OER/HER testing.

Fig. S14. Surface chemical oxidation states for $Co_{0.85}Ce_{0.15}$ analysed using XPS measurements before and after OER/HER testing: **(a)** deconvoluted Co 2p, **(b)** deconvoluted Ce 3d, and (c) deconvoluted O 1s.

(a)

KIST 10.0kV 5.3mm x30.0k SE(U) 1.00µm

(b)

KIST 10.0kV 4.7mm x30.0k SE(U) 1.00µm

(c)

KIST 10.0kV 4.5mm x30.0k SE(U) 1.00µm

Fig. S15. Morphological analysis of $Co_{0.85}Ce_{0.15}$ after long-term OER and HER stability testing: **(a)** before testing, **(b)** after the OER, and **(c)** after the HER.
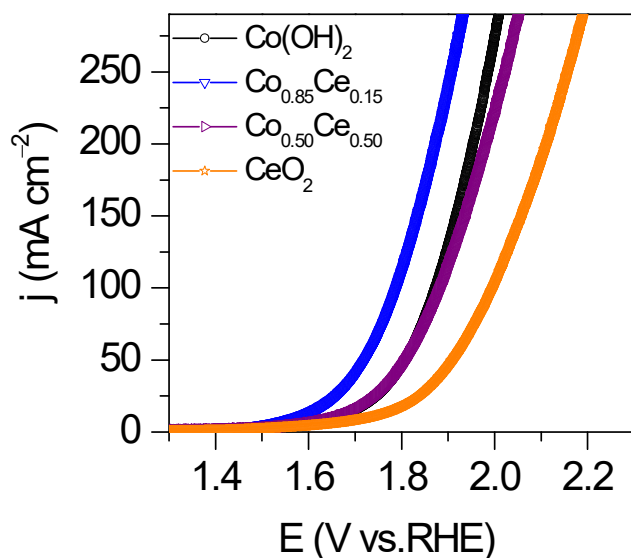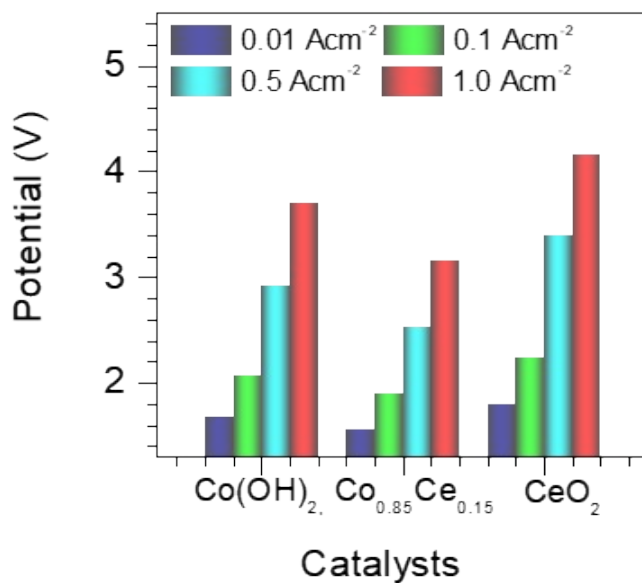
Fig. S16. Enlarged view of the polarization curves for the electrolysers fabricated using Co(OH)$_2$‖Co(OH)$_2$, Co$_{1-x}$Ce$_x$ ‖ Co$_{1-x}$Ce$_x$, (where x = 0.15, and 0.50) and CeO$_2$‖CeO$_2$ catalysts.
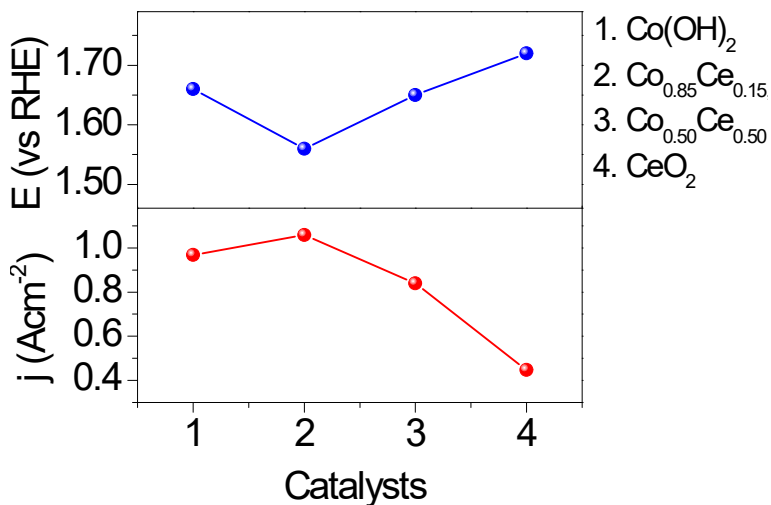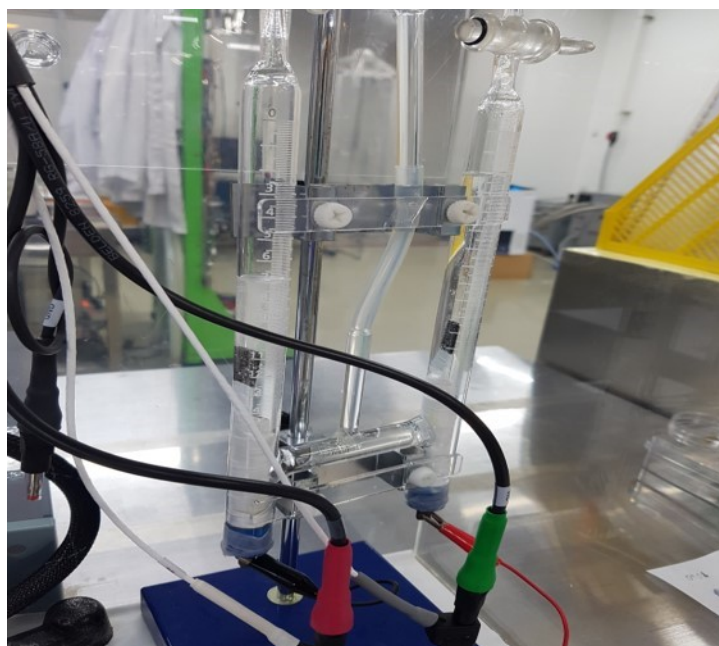

Fig. S17. Cell voltage required to reach a current density of 10 mAcm^{-2} and the maximum current density obtained for the Co(OH)$_2$, Co$_{1-x}$Ce$_x$, and CeO$_2$ catalysts.

Table S9. Full-cell parameters obtained for the electrolyser fabricated using the $Co(OH)_2$, $Co_{1-x}Ce_x$ (where x = 0.15, and 0.50), and CeO_2 catalysts

Sample	Cell Potential (V) @ $10mAcm^{-2}$	Cell Potential (V) @ $500mAcm^{-2}$	Cell Potential (V) @ $1000mAcm^{-2}$
$Co(OH)_2$	1.66	2.11	-
$Co_{0.85}Ce_{0.15}$	**1.56**	**2.05**	**2.27**
$Co_{0.50}Ce_{0.50}$	1.65	2.18	-
CeO_2	1.72	-	-

Fig. S18 Full-cell performance of $Co_{0.85}Ce_{0.15}$ compared with pure $Co(OH)_2$ and CeO_2 at a current density of 0.01, 0.1, 0.5, and 1.0 Acm^{-2}.

Fig. S19. Image of the experimental setup used to estimate the Faradaic efficiency by collecting the hydrogen and oxygen gas evolved at the cathode and anode, respectively.

Table S10. Cell voltage required to obtain a current density of 10, 500, and 1000 mAcm^{-2} at different temperatures for the electrolysers fabricated using the Co$_{1-x}$Ce$_x$ catalysts (where x = 0.05, 0.15, 0.25, and 0.50).

Temperature (°C)	Cell Potential (V) @ 10 mAcm^{-2}	Cell Potential (V) @ 500 mAcm^{-2}	Cell Potential (V) @ 1000 mAcm^{-2}
25	1.56	2.05	2.27
35	1.53	1.98	2.17
45	1.50	1.94	2.11
55	1.48	1.90	2.07

References

[S1] A. I. Inamdar, H. S. Chavan, S. M. Pawar, H. Kim. H. Im, *Int. J. Energy Res.* 2020, **44**, 1789-1797.

[S2] G. Zhang, Y. Meng, B. Xie, Z. Ni, H. Lu, S. Xia, *Appl. Catal. B: Environ.* 2021, **296**, 120379.